International Journal of Coal Geology 281 (2024) 104406

Contents lists available at ScienceDirect

International Journal of Coal Geology

journal homepage: www.elsevier.com/locate/coal

Combining atomic force microscopy and nanoindentation helps characterizing in-situ mechanical properties of organic matter in shale

Jianfeng Wang [a,b,c,d], Joanna Dziadkowiec [d,**], Yuke Liu [e], Wenmin Jiang [a,b], Yijun Zheng [a,b], Yongqiang Xiong [a,b,*], Ping'an Peng [a,b], François Renard [d,f]

[a] State Key Laboratory of Organic Geochemistry, Guangzhou Institute of Geochemistry, Chinese Academy of Sciences, Guangzhou 510640, China
[b] CAS Center for Excellence in Deep Earth Science, Guangzhou 510640, China
[c] University of Chinese Academy of Sciences, Beijing 100049, China
[d] The Njord Centre, Departments of Geosciences and Physics, University of Oslo, Blindern, 0316 Oslo, Norway
[e] Research Institute of Petroleum Exploration and Development, Beijing 100083, China
[f] ISTerre, Université Grenoble Alpes, Université Savoie Mont Blanc, CNRS, IRD, Université Gustave Eiffel, 38000 Grenoble, France

ARTICLE INFO

Keywords:
Organic matter
Wufeng-Longmaxi shale
In-situ
Nanoindentation
Atomic force microscopy
Mechanical properties

ABSTRACT

The quantification of mechanical properties of organic matter in shale is of significance for the fine prediction and characterization of shale reservoir's mechanical properties. Due to the micron-sized and dispersed distribution of organic matter particles in shale, the accurate evaluation of the actual mechanical response remains challenging. This work focuses on shale from Wufeng-Longmaxi Formation, which is the main shale gas exploration and development formation in China. A method based on atomic force microscopy (AFM) with an optical microscope (i.e., in-situ AFM technique) is presented to locate the organic matter in-situ and then visualize and quantify its mechanical properties using AFM Young's modulus mapping. The merits and limitations for determining the mechanical properties of organic matter in shale between the AFM and the more conventional nanoindentation technique are discussed. Results show that combining in-situ nanoindentation and in-situ AFM mapping provides more accurate description of the mechanical properties of organic matter in shale than traditional grid indentation methods with low spatial resolution. The Young's moduli of organic matter calculated from nanoindentation are around twice smaller than those obtained from AFM measurements mainly because the elasto-plastic deformation zone of organic matter in nanoindentation tests is larger and can be additionally affected by the presence of inorganic particles and/or larger micro-pores in organic matter. The Young's modulus and hardness of graptolite in the shale obtained by nanoindentation are slightly larger than those of solid bitumen at the same thermal maturity. Both in-situ AFM and in-situ nanoindentation results show that the mechanical strength of organic matter increases with increasing maturity. Overall, the presented approach shows a great potential for accurate and in-situ measurement of the mechanical properties of organic matter in shale at the nanoscale, which may be beneficial to the development of rock mechanical models for the accurate evaluation of the actual mechanical properties of shale.

1. Introduction

Shale is a common type of sedimentary rock encountered during field operations such as the hydraulic fracturing process, and can also serve as subsurface seals of CO_2 geological storage due to its low matrix permeability and high capillary entry pressure (Allen et al., 2020; Charlton et al., 2023). Measuring the mechanical properties of shale is of significance for successful oil and gas exploration and development and security implementation for CO_2 geological storage projects. Shales are highly heterogeneous and are mainly composed of various inorganic minerals, organic matter, and defects (pores and fractures) (Charlton et al., 2021; Davis, 1900; Du et al., 2021; Hutton, 1987; Mighani et al., 2019; Yang et al., 2020a, 2020b). For organic-rich shales, the content of organic matter can significantly affect the macro-mechanical properties,

* Corresponding author at: State Key Laboratory of Organic Geochemistry, Guangzhou Institute of Geochemistry, Chinese Academy of Sciences, Guangzhou 510640, China.
** Corresponding author.
E-mail addresses: joanna.dziadkowiec@fys.uio.no (J. Dziadkowiec), xiongyq@gig.ac.cn (Y. Xiong).

https://doi.org/10.1016/j.coal.2023.104406
Received 29 September 2023; Received in revised form 23 November 2023; Accepted 26 November 2023
Available online 30 November 2023

especially for shales with high total organic carbon content (TOC). For example, the Young's modulus of Bakken Formation shale in the bedding plane parallel direction decreases from 45.7 to 20.1 GPa when the TOC content increases from 7 to 20 wt% (Li et al., 2018a).

Organic matter in shale is present as micron-scale domains. Thus, conventional uniaxial/triaxial compression tests or ultrasonic pulse velocity tests cannot characterize the mechanical properties of organic matter components (Ahmadov et al., 2009). As a result, micro- and nano-mechanical characterization techniques, such as nanoindentation and atomic force microscopy (AFM), are widely used in materials science because they require small sample volumes only. They have been gradually introduced to measure mechanical data of organic matter in shale (Ahmadov et al., 2009; Eliyahu et al., 2015; Fender et al., 2020; Kumar et al., 2012; Li et al., 2018b, 2018c; Shukla et al., 2013; Tan et al., 2020; Vranjes-Wessely et al., 2021; Zeszotarski et al., 2004; Zhang et al., 2022).

Nanoindentation uses a low load of several mN onto a sample's surface and mechanical parameters (e.g., elastic modulus and hardness) can be obtained based on the load-displacement curve (Oliver and Pharr, 1992). Zeszotarski et al. (2004) first applied nanoindentation to measure the mechanical properties of kerogen in Woodford shale. Since then, several studies have applied the nanoindentation technique to measure the mechanical properties of micron-sized organic matter grains in shales (Ahmadov et al., 2009; Alstadt et al., 2015; Bennett et al., 2015; Khatibi et al., 2018; Kumar et al., 2012; Wang et al., 2022a, 2023; Zhao et al., 2020), coals (Hou et al., 2020; Kossovich et al., 2016; Vranjes-Wessely et al., 2018; Yu et al., 2018) and kerogen (Wang et al., 2022b). However, it is challenging to link each indent response with the presence of an organic matter grain because of the limited resolution of the nanoindenter's displacement, especially for small organic matter grains (usually <10 μm). More precise measurements of organic matter mechanical modulus is possible by combining grid nanoindentation with a deconvolution method (Ahmadov et al., 2009; Bennett et al., 2015; Kong et al., 2021; Slim et al., 2019). This method requires to locate the organic matter grains and to apply a large number of indents on shale's surface that contains the organic matter area; however it is time-consuming and may not be statistically significant for small, micron-sized organic matter domains. Another method to acquire nanoscale mechanical data on organic matter is to indent the surface of organic matter grains only, without indenting any other mineral phase in shale. A nanoindenter equipped with a high-resolution optical microscope and large size of organic matter grains are indispensable for this method.

When considering the AFM technique, PeakForce Quantitative Nanomechanical Mapping (PF-QNM) and Quantitative Imaging AFM (QI-AFM) provide suitable solutions for organic matter mechanical studies (Eliyahu et al., 2015; Fender et al., 2020; Graham et al., 2021; Zargari et al., 2016). One can calculate the elastic modulus of the organic matter from data with nanometer resolution, based on continuum mechanics models (Derjaguin et al., 1975; Sneddon, 1965). Similar to the grid nanoindentation method, this method requires probing a large area within the located organic matter region. However, to the best of our knowledge, few studies conducted the organic matter-positioned AFM mechanical analysis (Zhang et al., 2022), which assures that the indents from AFM tip act only on the organic matter domain in shale.

Type, thermal maturity and pore characteristics of organic matter in shale affect its mechanical response. However, it is not fully understood how these properties influence the mechanical properties of shales. For example, it has been reported that the elastic modulus of kerogen in the Bakken shale decreases with maturity from immature to mature stages (Zargari et al., 2016), while latest studies show the opposite results for the organic matter from the Bakken shale (Khatibi et al., 2018; Li et al., 2018b). Some works show even more complex dependence where the elastic modulus of organic matter generally decreases with increasing maturity (from 1.33 to 1.96% vitrinite reflectance, R_o), and then increases slightly between 2.00 and 2.23% R_o from the Lower Cretaceous Shahezi Formation rock in the Songliao Basin, China (Vranjes-Wessely et al., 2021). For the different kinds of organic matter in the same shale, it is reported that the elastic modulus of kerogen is larger than that of bitumen (Vranjes-Wessely et al., 2021; Zargari et al., 2013; Zhao et al., 2020). At the same maturity level ($R_o = 1.10\%$), the stiffness of organic matter of lacustrine shales in Shahejie Formation, Bohai Bay Basin, China follows: fusinite > inertinite (macrinite) > micrinite > vitrinite (Gao et al., 2023). The Wufeng-Longmaxi (WF-LMX) shales are all in an over-mature stage with $R_o > 2.0\%$, the main organic matter are graptolite and solid bitumen (SB), the characteristics of organic pores vary greatly (Yang et al., 2020b; Yang et al., 2016), and the optical characteristics of these organic matters can also vary at different bedding plane (Goodarzi, 1984). How these factors influence the mechanical properties of organic matter in WF-LMX shales is poorly understood.

In this work, a method combining AFM with optical microscopy to locate the organic matter in-situ is developed, which quantifies its mechanical properties, and uses the nanoindentation technique to obtain the elastic modulus of organic matter in-situ in shale. Here, seven marine, over-mature WF-LMX Formation shale samples were selected. The main goals of this study are to 1) locate and identify the organic matter, and calculate the Young's modulus of the organic matter in shale with AFM and nanoindentation at the nano- and micro-scale, 2) examine the factors that influence the mechanical properties of organic matter in shale, and 3) further compare the mechanical responses obtained by the two techniques, and assess the advantages and limitations of nanoindentation and AFM for obtaining the organic matter's elastic response.

2. Materials and methods

2.1. Shale samples

Seven shale core samples, named SQ-61, SQ-81, SQ-85, SQ-86, SQ-88, SQ-89, and AW-105, were respectively collected from two shallow vertical boreholes drilled in Sanquan Town and Anwen Town of the Chongqing city, Sichuan Basin, South China. These shales belong to the Upper Ordovician Wufeng Formation–lower Silurian Longmaxi Formation (i.e., the WF–LMX shales). This formation shale displays good exploration prospects towards shale gas (Guo and Zhang, 2014; Yang et al., 2016). The same shale samples were used in previous studies (Yang et al., 2020a; Zheng et al., 2018). The mineralogical, organic, and porosity parameters are summarized in Table 1. The R_O values are all larger than 2.0%, showing that these shale samples are in an over-mature stage. The TOC content suggests that all the shale samples are organic-rich except sample SQ-61.

The shale samples were cut both perpendicular (X1) and parallel (X3) to the bedding plane for SQ-89, and parallel (X3) to the bedding plane for the other samples. The samples were first cut the samples into 1–10 mm thick chips, impregnated with epoxy resin, and further were ground and polished with silicon carbide abrasive papers of different grain sizes (mesh numbers from 50 to 2000 grit). Then, 9, 3, and 1 μm diamond suspension fluids for fine polishing were successively used (Yang et al., 2020a). Finally, an IM4000 argon ion mill was used to polish the sample surface for 2 h. The mean roughness (root mean square roughness, R_q) measured in two different areas (30 × 30 μm^2) of the shale surface with an AFM, was <100 nm (Wang et al., 2022c). Nanoindentation data were acquired on organic matter grains identified with the optical microscope for all the thin sections. In contrast, the AFM apparatus has a lower resolution optical microscope and we acquired AFM data on samples SQ-81, SQ-86, SQ-88, and SQ-89 only.

2.2. Nanoindentation measurements

The nanoindentation tests were conducted with an Anton Paar TTX NHT^3 nanoindenter, which is equipped with a diamond Berkovich tip with a radius of curvature of 50–100 nm. The indentation system has a high-resolution optical microscope (a maximum magnification of 4000×), making it possible to observe the surface location clearly before

Table 1
Organic material, mineralogical, and porosity properties of shale core samples. N/A: Not Available.

Sample	Depth (m)	Organic parameters		φ (%)	Mineralogical compositions based on XRD (vol%)					
		VR_o (%)	TOC (wt%)		Qtz	Cly	Fs	Cal	Dol	Py
SQ-61	60.9	2.14	1.18	2.2	27	42.5	20.1	2.9	2.2	5.3
SQ-81	81.1	2.56	2.71	N/A	34.5	38.5	17.3	3.9	3.7	2.1
SQ-85	85.4	2.38	6.53	4.12	44.4	31.2	13.3	2.9	2.3	5.9
SQ-86	86.4	2.65	4.41	4.66	51.5	28.8	12.5	3.2	2.2	1.8
SQ-88	88.3	2.76	3.45	N/A	29.3	48.1	14.5	2.8	2.2	3.1
SQ-89	89.1	2.60	3.29	2.94	34.4	45.9	13.6	2.7	1.8	1.6
AW-105	105.7	3.10	6.87	N/A	31.3	39.9	14.0	1.9	3.6	9.3

Note: Porosity = φ; Cly = clay; Quartz = Qtz; Feldspar = Fs; Calcite = Cal; Dolomite = Dol; Pyrite = Py; VR_o = equivalent vitrinite reflectance. $VR_o\% = (BR_o\% + 0.2443)/1.0495$ (Schoenherr et al., 2007). $BR_o\%$ = solid bitumen reflectance.

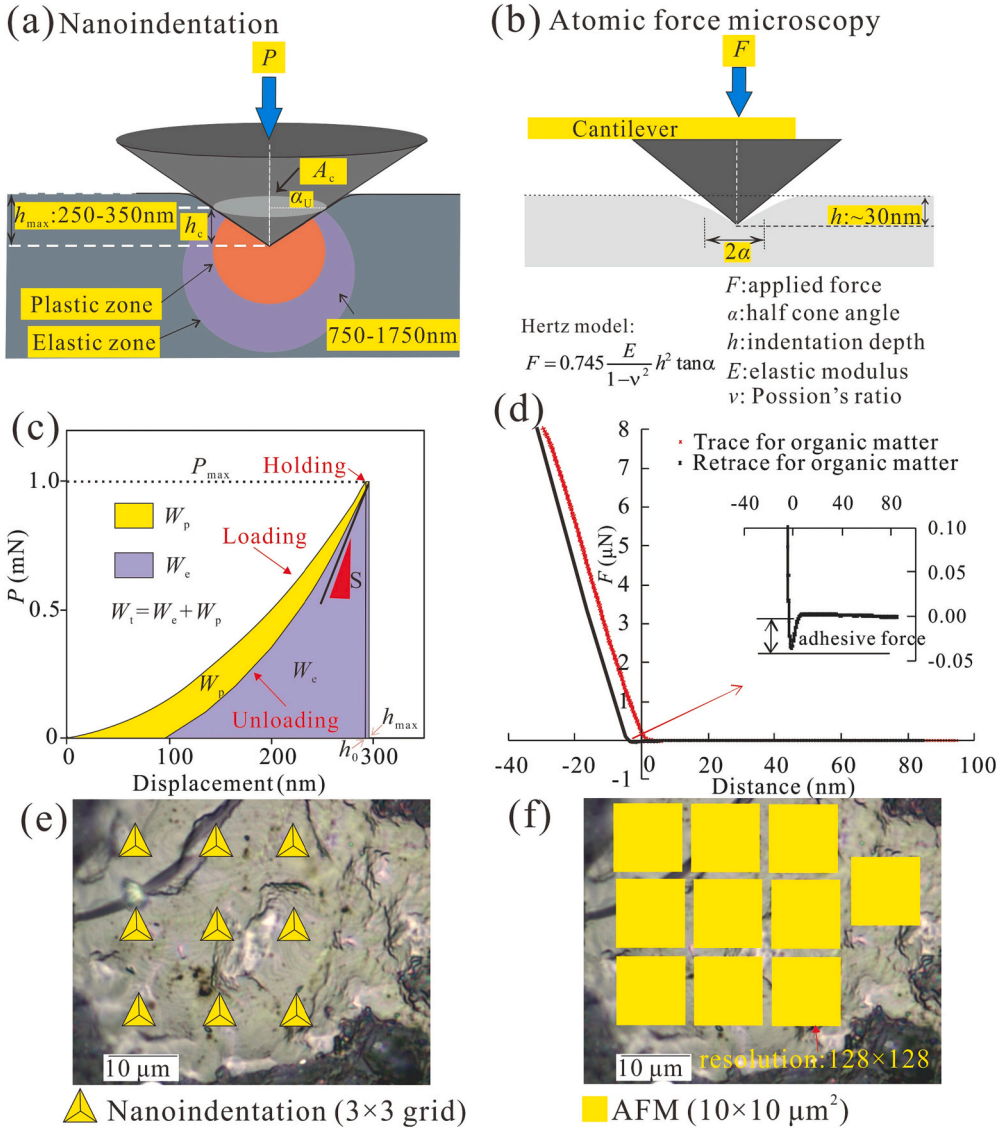

Fig. 1. (a) Schematic diagram of a nanoindentation test and (b) atomic force microscope (AFM) force spectroscopy test; (c) typical load–displacement (*P*-*h*) curve from nanoindentation test and (d) representative force-distance curve from our AFM mechanical test for organic matter; (e) schematic of nanoindentation grid, and (f) AFM mapping on organic matter, with each yellow box representing an AFM Young's modulus map. For nanoindentation: *P* is the applied load, P_{max} is the peak load, α_u is the contact radius, *S* is the contact stiffness, *h* is the indentation displacement, h_0 and h_{max} are the displacement at the beginning of the holding stage and the maximum displacement during nanoindentation, respectively. Elastic-plastic deformation zone beneath the indenter is 750–1750 nm for organic matter. W_e is the elastic work and W_p is the plastic work. The total work (W_t) is equal to the sum of W_e and W_p. For AFM test: *h* is the indentation depth and is equal to ~30 nm for organic matter in shale, yielding a minimum indentation zone width of approximately 20 nm. The enlarged part in (d) shows the adhesive force of the organic matter is <50 nN. We acquired point measurements on a grid, which size was adjusted to the size of a given organic matter domain in order to maximize the number of indents (e.g., 3 × 3, 3 × 4, or 5 × 2) using nanoindentation (e) and scanned ten AFM maps with dimension 10 × 10 μm^2 with 128 × 128 indents for each acquired AFM map (f). (For interpretation of the references to colour in this figure legend, the reader is referred to the web version of this article.)

the nanoindentation tests were conducted (Wang et al., 2022a; Yang et al., 2020a). The magnification/numerical aperture parameters of the optical objectives are 5×/0.10, 20×/0.40, 50×/0.75, and 100×/0.90, respectively.

Before the nanoindentation tests, we used a standard fused silicon specimen to calibrate the tip shape. Fig. 1a displays a schematic diagram of the nanoindentation. Fig. 1c shows a typical load–displacement curve (*P*–*h* curve), which contains loading, holding, and unloading stages. The loading stage records elastic and plastic deformations whereas the unloading stage records elastic deformation only. Based on *P*–*h* curve, the reduced Young's modulus (E_r) and hardness (H) of a sample can be obtained:

$$E_r = \frac{S\sqrt{\pi}}{2\beta\sqrt{A_c}} \tag{1}$$

$$H = \frac{P_{max}}{A_c} \tag{2}$$

where the stiffness of the material, S, is determined from the slope of the initial unloading curve, β (a constant that depends on the geometry of the indenter) is equal to 1.034 for the Berkovich indenter, and A_c is the projected contact area, which is calculated from the contact displacement (h_c) (Oliver and Pharr, 1992, 2004).

According to the reduced Young's modulus (E_i) and Poisson's ratio (ν_i) of the diamond indenter, the Young's modulus (E) of the sample can be calculated as:

$$\frac{1}{E_r} = \frac{1-\nu^2}{E} + \frac{1-\nu_i^2}{E_i} \tag{3}$$

where $E_i = 1140$ GPa and $\nu_i = 0.07$, respectively. E and ν are the Young's modulus and Poisson's ratio of the samples to be tested, respectively. In this study, the Poisson's ratios of the organic matter were assumed equal to 0.3 (Li et al., 2018a; Zhao et al., 2020). If the Poisson's ratio varied between 0.05 and 0.45 for organic matter, it would result in an uncertainty of 12.4% on the measured Young's modulus (Zhao et al., 2020).

The constant load holding tests were applied at room temperature for all the samples. A peak load of 1 mN for nanoindentation tests was used. The indentation test was loaded and unloaded over 30 s. The diamond indenter was held for a period of 2 s to avoid creep effects for the holding stage. Before each test, we observed the surface of the rock via the high-resolution optical microscope to select the areas with organic matter. Organic matter grains with similar surface area and reflective characteristics were selected in the WF-LMX shales under the nanoindenter's optical microscope (Yang et al., 2023). A suitable grid dimensions (typically 3 × 3 or 3 × 4) with the distance between neighboring indents of 10 μm was used to conduct the nanoindentation tests (Fig. 1e). As determined from neighboring indents, this load can produce the displacement of ~250 nm and the indent size of ~1 μm. The indents that did not act on the organic particles after tests were discarded.

2.3. Atomic force microscopy measurements

2.3.1. Principles and test procedure

Nanomechanical measurements were performed with a JPK NanoWizard atomic force microscope equipped with a top-view Olympus IX71 optical microscope, with a maximum magnification of 20×. The nanomechanical data was extracted from force curves obtained in the quantitative imaging (QI™) mode developed by JPK, and referred to here as QI-AFM. In the QI-AFM mode, a complete force curve for a given z length and load setpoint is measured at each scanned pixel of the image. During the acquisition of force curves, the off-resonant motion of the cantilever is linear with no lateral XY movement, which helps achieving a constant speed of the cantilever. Such tip movement ensures that no lateral forces are applied to the sample while scanning on its topographical features and is vital to obtain meaningful information about the sample's mechanical properties (Fig. 1b).

The high-stiffness antimony-doped silicon RTESPA-525 AFM tip probes supplied by Bruker were used to acquire AFM nanoindentation force curves. These tips were selected because of their high nominal spring constant of 200 N m^{-1}, which is suitable for samples with moduli of approximately 20 GPa (Lévy and Maaloum, 2002). Before each measurement on a shale sample, we first calibrated the spring constant of a given AFM probe using the built-in thermal tune calibration method. Then, the tip sensitivity was determined on a highly-ordered pyrolytic graphite (HOPG) standard with a Young's modulus of 18 GPa, supplied by JPK. For that, three force maps in three various locations on the pyrolytic graphite standard surface over a map of 128 × 128 pixels were acquired with a set point of approximately 8 μN, z length of 400 nm, a displacement velocity of 25 μm/s, and a scan size of 10 × 10 μm^2 (Liu et al., 2020). The extend parts of the measured force-distance curves were then processed in the JPK analysis software, performing baseline correction, contact point definition, and tip-sample separation calculation. The processed force curves could be then fit with the Hertz-Sneddon elasticity model (Hertz, 1882; Sneddon, 1965) (full fit for force curves with the applied load set-point of 8 μN) until the sensitivity was tuned to yield the average Young's modulus of the given force map close to 18 GPa. The tip sensitivity used in the further measurements on the shale samples was the average value of the fitted sensitivities on the three acquired force maps. The fit parameters were indenter geometry with triangular pyramid of 17.5° angle and Poisson's ratio of both the HOPG standard and organic matter in shale was set equal to 0.3 (Zhao et al., 2020).

After this crucial sensitivity calibration step, the Young's modulus on a given shale sample was measured using the same calibrated AFM tip. Similar to the nanoindentation test, the surface of the shale via the AFM-attached, top-view optical microscope was observed in order to locate the target organic matter before the nanomechanical tests. Because of the similar reflection colors between organic and hard minerals (e.g., quartz and feldspar) as viewed in our AFM's microscope, some of the grains were quickly scanned with AFM to ensure that they contain organic matter. Then, a large area (~100 × 100 μm^2) under QI mode with a low pixel resolution of 64 × 64 was scanned to precisely locate the organic matter. Once we found a reasonably large patch of organic matter, a 10 × 10 μm^2 non-overlapping area within this patch were probed under QI mode with a map size of 128 × 128 indents, which gives a distance between the indents of ~78 nm and a minimum indentation zone width of ~20 nm, calculated assuming a conical AFM tip geometry. Fig. 1d shows a representative force-distance curve from AFM test for organic matter. For each organic matter patch, we acquired ten AFM maps (Fig. 1f). To obtain the spatially resolved Young's moduli, the force maps were then processed using the JPK software similarly to those measured on the pyrolytic graphite standard, with the calibrated tip sensitivity value as an input parameter.

In the used Sneddon's modification of Hertz model of contact mechanics using JPK Data Processing software was employed (Hertz, 1882; Sneddon, 1965). In this model, Young's modulus (E) for triangular pyramid indenter in the Hertz model is calculated by:

$$F = 0.745\frac{E}{1-\nu^2}h^2 tan\alpha \tag{4}$$

where F is the force in nN; ν is the Poisson's ratio; h is the indentation depth in nm, and α is the half cone angle.

Adhesion (pull-off force) data were obtained from the analysis of the retract part of force-distance curves by using JPK Data Processing software as the maximum negative force before the adhesive jump-out from the contact, as shown in Fig. 1d.

2.3.2. Roughness analysis

The mean roughness (R_a) and root mean square roughness (R_q) are common parameters used to evaluate surface roughness (Abouelatta and

Mádl, 2001; Gadelmawla et al., 2002). R_a is defined as the arithmetic mean of the absolute value of the height deviation measured relative to the central plane in the tested area, and R_q is the standard deviation of the surface height distribution, which can be calculated as follows (Abouelatta and Mádl, 2001):

$$R_a = \frac{1}{N_x N_y} \sum_{i=1}^{N_x} \sum_{j=1}^{N_y} |z(i,j) - z_{mean}| \quad (5)$$

$$R_q = \frac{1}{N_x N_y} \sum_{i=1}^{N_x} \sum_{j=1}^{N_y} (z(i,j) - z_{mean})^2 \quad (6)$$

$$z_{mean} = \frac{1}{N_x N_y} \sum_{i=1}^{N_x} \sum_{j=1}^{N_y} z_{ij} \quad (7)$$

N_x and N_y are the number of scanning points on the x-axis and y-axis of the AFM images, respectively. Z (i, j) is the height of the (i, j) measuring point, and Z_{mean} is the mean height of all the scanning points of the AFM image. The roughness parameters were extracted from the same force maps as the ones used for the Young's modulus determination, using the RTESPA-525 AFM tips.

3. Results

All seven samples (SQ-61, SQ-81, SQ-85, SQ-86, SQ-88, SQ-89, and AW-105) were used for the nanoindentation tests and four samples (SQ-81, SQ-85, SQ-88, and SQ-89) were used for the AFM measurements. Nanoindentation data contain optical micrographs, indentation response, and mechanical properties of different patches of organic matter. AFM data comprise optical micrographs, pore morphology and surface roughness data, mechanical and adhesion properties of organic matter.

3.1. Nanoindentation results

3.1.1. Identification of organic matter types

Two main types of organic matter in the WF-LMX Formation shales are graptolites and solid bitumen. Graptolites, generally occur as fragments, which are spread in shale, and the graptolite domain size (>10 μm) is usually larger than that of solid bitumen (Figs. 2a- 2p). Most graptolites are not fully preserved. A small number of graptolites have lath-like characteristics (Fig. 2a, b), and some have preserved the original symmetric shell shape of graptolites. It is generally proposed that the fragments of graptolites observed under an optical microscope mostly come from their peridermal tissues (Fig. 2a, b), because they are

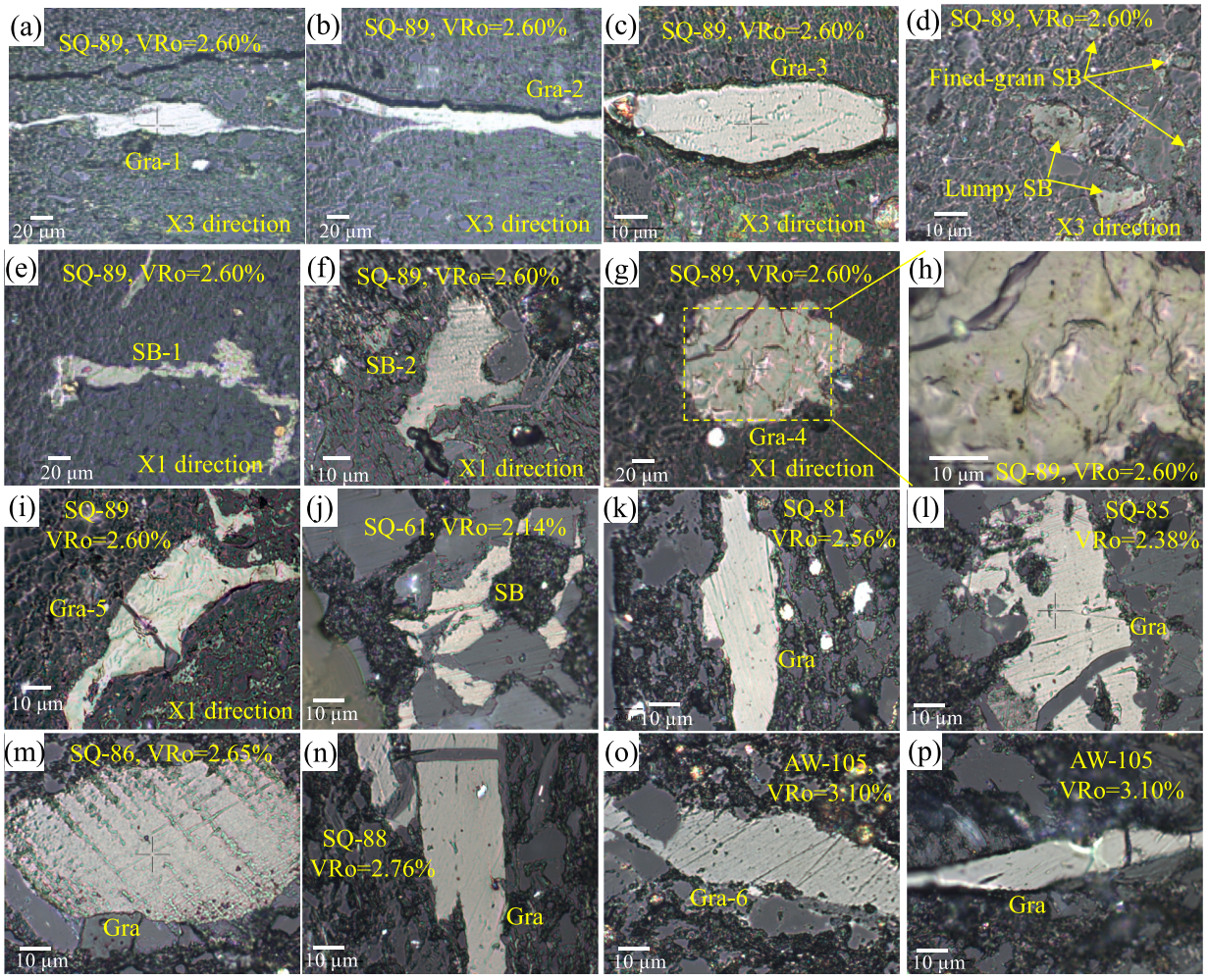

Fig. 2. Morphological and reflective characteristics of graptolite and solid bitumen in shales under the nanoindenter's optical microscope. (a, b, c, i, k, l, n, o, p). Non-granular graptolites display smooth surface and high reflectivity, and (g, m) granular graptolites show weaker reflectivity and larger surface granularity. (d, e, f, j) solid bitumen show relatively low reflectivity; the particle sizes of solid bitumen are smaller than that of graptolites. (d) solid bitumen contains the lumpy solid bitumen and fine-grained solid bitumen. (a-d) and (e-i) are from SQ-89 at X3 direction and X1 direction, respectively. (j) shows solid bitumen from SQ-61, (k), (l), (m), (n), and (o-p) show graptolites from SQ-81, SQ-85, SQ-86, SQ-88, and AW-105, respectively. Graptolites = Gra. Solid bitumen = SB.

relatively difficult to hydrolyze and can be maintained during the burial of the shale (Link et al., 1990). Graptolite particles can be divided into two forms: granular or nongranular. The surface of granular graptolites has a fine-grained to network structure (Fig. 2g, h, and m), with an overall elliptical shape and a rough surface, exhibiting weaker anisotropy. Its texture is soft and exhibits low reflectivity (Goodarzi, 1984). The organic matter grain granular graptolites-4 show very weak reflectivity and great surface granularity (Fig. 2g-2h). Non-granular graptolites are relatively hard, brittle, and exhibit high reflectivity, with strong optical anisotropy (Goodarzi, 1984). Non-granular graptolites are easier to distinguish (Fig. 2a, b, c, i, k, l, n, o, and p), while the optical characteristics of granular graptolites are similar to those of lumpy solid bitumen (i.e., pyrobitumen) (Fig. 2d). The main difference is that granular graptolites have a graptolite shape, while lumpy solid bitumen does not exhibit a clear shape.

Solid bitumen (SB) has different forms, including granular, microsome, nano-porous, dispersed matrix, homogeneous lump, etc. Solid bitumen in the WF-LMX Formation shale can generally be divided into two types: one is lumpy solid bitumen (i.e., pyrobitumen) with high reflectivity, and the other is matrix solid bitumen (e.g., fine-grained solid bitumen) with low reflectivity (Fig. 2d). Lumpy solid bitumen is a block angular organic matter particle that fills around the edges or in the pores of mineral particles (Fig. 2d, e, f, and j). It has a relatively uniform texture, clear outline, and particle size is generally from <1 μm to >10 μm, but most of them are within 10 μm (Fig. 2d). The matrix solid bitumen is in the form of filamentous, diffuse, flocculent, ribbon and other dispersed amorphous solid forms, mainly distributed in pores or fractures (Fig. 2d), and its shape changes with the shape of pores or fractures, and can also be filled in the mineral matrix as a fine mesh (Bertrand, 1987). Besides, organic matter, such as marine vitrinite and chitinozoan, has been previously detected in marine shales (Bertrand, 1987; Yang et al., 2020b). This type of organic matter in our samples of WuFeng-Longmaxi shale samples was however not identified.

3.1.2. Indentation response and mechanical properties of different types of organic matter

After the identification of the type of organic matter, the nanoindentation tests were conducted on the selected organic matter grains. Fig. 3a summarizes the representative load-displacement curves of the different types of organic matter shown in Fig. 2. Overall, under a load of 1 mN, the maximum displacement in solid bitumen is larger than in graptolite, suggesting that solid bitumen has a compressibility higher than graptolite. The size of solid bitumen grains (Fig. 2d) is too small to be located and tested by our nanoindenter.

The mechanical properties obtained for different types of organic matter for sample SQ-89 are shown in Table 2. The Young's modulus and hardness values of organic matter are larger for graptolite than for solid bitumen. The standard deviation of Young's modulus and hardness for Gra-4 and Gra-5 are relatively much larger than those from other organic matter grains, mainly due to their internal heterogeneity. The mechanical properties obtained for granular and non-granular graptolite particles are relatively close, suggesting that the granularity of graptolites has little effects on the calculated Young's modulus and hardness values. The mechanical properties of graptolite particles on the X1 and X3 bedding planes are relatively similar. Also, solid bitumen displays similar Young's modulus and hardness values in X1 bedding plane.

X1 and X3 indicate direction perpendicular and parallel to the bedding plane, respectively. Graptolites: Gra; solid bitumen: SB; Gra-1, Gra-2, Gra-3, Gra-4, Gra-5, SB-1 and SB-2 are the corresponding organic matter grain in Fig. 2. *n*: the respective number of measurements.

Overall, the Young's moduli values of both graptolite and solid bitumen vary in the range 5.7–6.5 GPa, and their hardness varies in the range 0.41–0.77 GPa, indicating that the different tested types of organic matters have similar mechanical properties (except SB-2), as determined by the nanoindentation technique. On the other hand, the W_e/W_t value of graptolites (i.e., 64.8–69.4%) is higher than that of solid bitumen (i.e., 62.6% and 50.1%), indicating a higher elastic recovery. Therefore, similar to kerogen at high-over maturity stages (Easy$R_o \geq$ 2.1%), no indentation marks were observed on the surfaces of solid bitumen and graptolites.

3.1.3. Mechanical properties for organic matter at different maturities

Fig. 2 shows nanoindenter's optical microscope images of organic matter at different maturities. The selected organic matter domains in WF – LMX shale exhibit dispersed (Fig. 2j), banded (Fig. 2k and n), or agglomerated (Fig. 2m) characteristics, showing yellow white colour under indentation microscope, and the main particle size is 10–50 μm (suitable for nanoindentation experiments). Due to the close mechanical properties of solid bitumen and graptolite discussed in Section 3.1.2, we did not distinguish the type of organic matter here. Because of the low TOC content in the SQ-61 sample, the organic matter particles found are relatively small. To prevent the influence of mineral matrix boundaries, we conducted statistical analysis on five indents, and the selected positions of the indents are avoided to locate at the edge of organic matter particles.

Fig. 3b summarizes the representative load-displacement curves of organic matter at different maturities. Overall, under a load of 1 mN, the indenter acts on relatively low maturity SQ-61 produces larger displacement of organic matter. Similarly, it can be observed from the curve that the elastic recovery for organic matter at different VRo is relatively high and close, which can be reflected by the quantitative ratio of W_e/W_t (55.8–69.4%) in Table 2. This indicates that the elasticity of the organic matter in the WF-LMX Formation shale is very high. The type of unloading curve is relatively close to that of anthracite (Kossovich et al., 2016), indicating that, the degree of graphitization is very high for the organic matter in WF-LMX Formation shale.

Fig. 4 and Table 2 show that with increasing maturity, the Young's modulus and hardness values of organic matter in the WF-LMX Formation generally show an upward trend, while the changes in these values

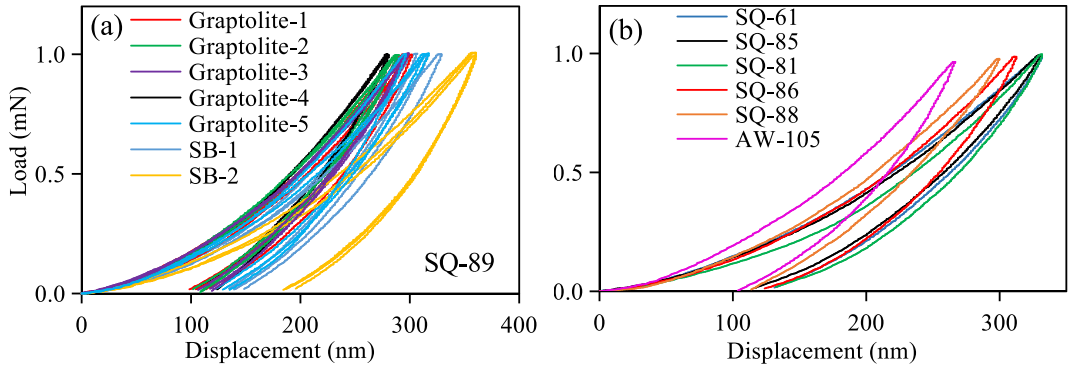

Fig. 3. Representative load-displacement curves for (a) various organic matter grains in sample SQ-89 and (b) organic matter in various shale samples.

Table 2
Mechanical properties of organic matter (graptolite and solid bitumen) in shale.

Sample	VR_o (%)	Bedding plane	Organic matter type	*E* (GPa)		*H* (GPa)		*We/Wt*(%)		*n*
				Ave.	Std.	Ave.	Std.	Ave.	Std.	
			Gra-1	6.4	0.1	0.73	0.03	69.0	1.8	8
		X3	Gra-2	6.5	0.3	0.77	0.03	69.4	1.3	10
			Gra-3	6.0	0.2	0.74	0.09	67.0	5.0	8
SQ-89	2.60		SB-1	6.1	0.3	0.61	0.05	62.6	2.6	8
		X1	SB-2	5.7	0.6	0.41	0.04	50.1	4.1	9
			Gra-4	6.2	0.7	0.73	0.12	67.2	1.8	8
			Gra-5	6.2	1.0	0.65	0.10	64.8	4.7	12
SQ-61	2.14	X3	SB	5.6	0.3	0.55	0.06	65.0	4.9	5
SQ-81	2.56	X3	Gra	6.0	0.2	0.60	0.07	67.8	3.5	7
SQ-85	2.38	X3	Gra	5.5	1.1	0.58	0.06	65.1	3.2	12
SQ-86	2.65	X3	Gra	6.6	0.3	0.66	0.04	66.7	3.4	9
SQ-88	2.76	X3	Gra	6.5	0.4	0.66	0.09	62.0	6.5	11
AW-105	3.10	X3	Gra-6	8.6	0.4	0.69	0.04	55.8	2.5	14

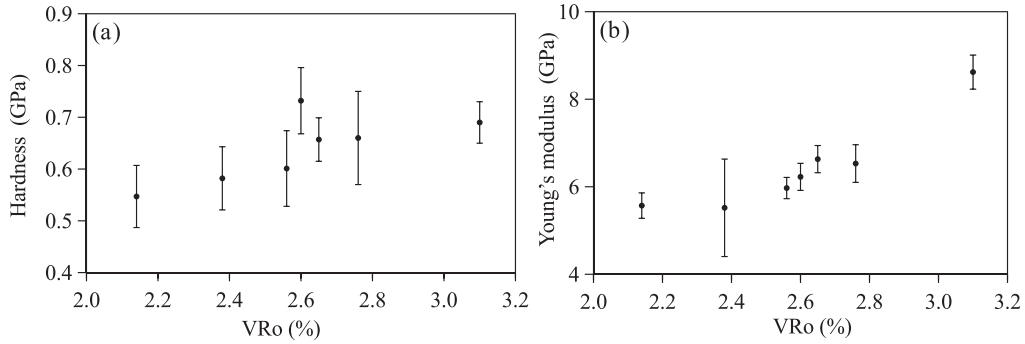

Fig. 4. Plots of hardness (a) and Young's modulus (b) with respect to maturity. We calculated the mean Young's modulus and hardness of Gra-1, Gra-2, Gra-3 of SQ-89 (i.e., VR_o = 2.60%), corresponding to the X3 direction in Table 2, to draw this figure.

are not significant. Specifically, the Young's modulus increased from 5.6 ± 0.3 GPa at VR_o = 2.14% to 8.6 ± 0.4 GPa at VR_o = 3.10%, and the hardness increased from 0.55 ± 0.06 GPa at VR_o = 2.14% to 0.69 ± 0.04 GPa at VR_o = 3.10%.

3.2. AFM results

3.2.1. Mechanical properties and adhesive force of organic matter assessed with AFM

The nanomechanical properties of organic matter domains within shale were assessed using a relatively novel in-situ approach based on AFM mapping with nanoscale resolution, which ensures no interference from other mineral phases. Fig. 5 shows representative optical images, surface roughness, the trend of changes in the values of surface roughness, Young's modulus, and pull-off adhesive force with VR_o for one organic matter domain in the four probed shale samples. Fig. 5a displays the optical images of organic matters from AFM microscope. According to the identification method from Section 3.1.1, what we can ensure is that the organic matter with slightly high VR_o (2.6, 2.65, and 2.76%) are graptolites, while the organic matter with lower VR_o (i.e., 2.56%) may be solid bitumen. Because of the close mechanical properties of solid bitumen and graptolite (Table 2), we discussed the mechanical properties of organic matter from AFM data without distinguishing the type of them. The large area (~100 × 100 μm^2) under QI mode with a map resolution of about 64 × 64 pixels was scanned to locate the organic matter (Fig. 5b). Among the four shale samples, with the increase of equivalent vitrinite reflectance VR_o, the roughness parameters R_a (from 3.4 to 10.2 nm) and R_q (from 4.5 to 13.0 nm) show a generally increasing trend. SQ-89 (VR_o = 2.60%) has much more micropores, while SQ-86 (VR_o = 2.65%) is rich in microcracks (Fig. 5b and c). The Young's moduli exhibit an upward trend with increasing VR_o. Specifically, it increases from 9.3 ± 1.5 GPa at VR_o = 2.56% for SQ-81 to 12.4 ± 2.0 GPa at VR_o = 2.76% for SQ-88 (Fig. 5d), which is consistent with our nanoindentation results. The corresponding adhesive forces show an upward trend with increasing VR_o from 2.56% to 2.76% in the shale samples (Fig. 5d and Table 3). The standard deviation of adhesive force shows a relatively large value, suggesting that the adhesion is more sensitive to reveal nanoscale heterogeneities on samples, especially local surface conditions. The change trend of R_a, R_q, Young's modulus, and the adhesion with VR_o can also be confirmed by the mean values calculate on the ten maps (Table 3). The surface adhesive force reflects the surface energy, and thus the adsorbability of the material to the surface gas (Li et al., 2020; Sauerer et al., 2016; Tian et al., 2022). The organic matter in four samples except SQ-81 have high adhesive force (Figs. 5e). This result suggests that the high adhesive force on the organic matter micro-surface may provide good mechanical conditions for the stable storage of shale gas.

Fig. 6 shows histograms of the Young's modulus measured for ten different areas of the organic matter in four different shale samples. The Young's modulus values are distributed relatively uniformly for all samples, with the lowest standard deviation of ten average Young's modulus values calculated for the sample SQ-88. This result indicates that the organic matter domains, which can extend over 100 μm are relatively homogenous in our shale samples, especially for sample SQ-88 (see Table 3). Individual Young's modulus maps generally show higher standard deviation values representing variation in all measurements collected for one map (see Table 3).

AFM mapping can additionally provide nanoscale information about the pore parameters (e.g., pore size, and pore plane porosity) of shale or coal (Zhao et al., 2019; Li et al., 2020). As such, pore characteristics of the tested organic matter domains were analyzed as shown in Supplementary Fig. S1. The identified pores display similar orientation and the pore size can be up to 2000 nm (Fig. S1), which cannot be observed by

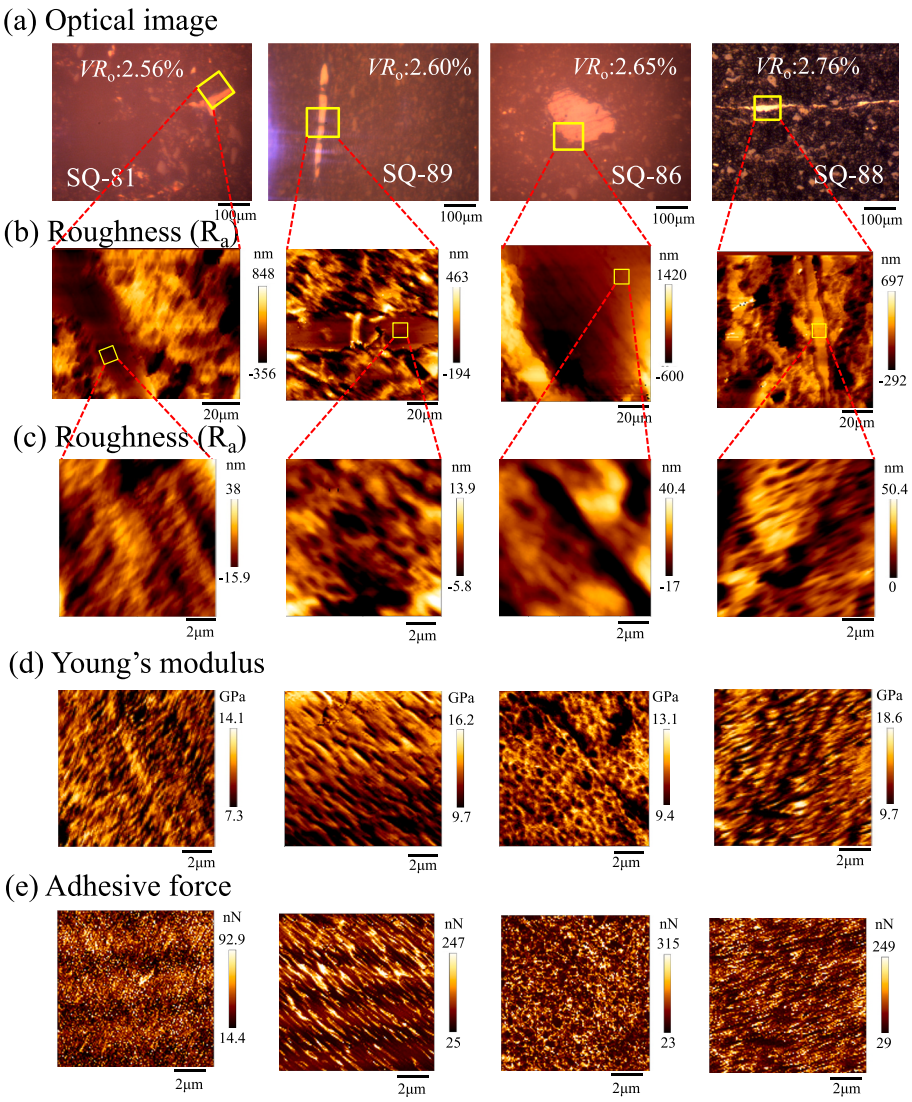

Fig. 5. (a) Optical microscope images of organic matter acquired using an AFM apparatus, and the corresponding VR_o values of the organic matter from left to right are 2.56%, 2.60%, 2.65%, and 2.76%; corresponding variations in roughness (R_a) for the area of (b) ~100 × 100 μm^2 and (c) 10 × 10 μm^2, in which developed micropores or microcracks are easily observed, scanned by AFM (map size of 128 × 128 pixels); (d) corresponding Young's modulus (determined by Hertz model) images with VR_o from 2.56% to 2.76%; (e) corresponding adhesive force images with VR_o from 2.56% to 2.76% in over-matured shale samples. Note: the organic matter in the first illustration in (a) is solid bitumen or graptolite, and the rest are graptolites. The yellow boxes represent the enlarged part. (b) shows the specific AFM scanning area from (a). (c), (d), and (e) are the same microscopic region for organic matter. The reported values are shown for one chosen representative AFM for one sample (see summary in Table 3). (For interpretation of the references to colour in this figure legend, the reader is referred to the web version of this article.)

our nanoindenter's optical microscope. The plane porosity value (~10–14%) determined from our AFM method is much larger than those from the whole rock porosity values typically <7%, with quite high and mean pore diameters that are not typical for organic matter in shale at this stage of maturity (Table S1 and Fig. S2). We therefore interpret that the orignal porosity of the organic matter was altered during sample preparation and partially represents ion milling induced artifacts (Fig. S3), which have been identified in previous studies (Valentine and Hackley, 2023). The reported AFM roughness values are also the outcome of the applied surface preparation process (Table 3, Fig. 5c).

4. Discussion

Our work presents complementary measurements of the mechanical response of organic matter within WF-LMX shale using in-situ nanoindentation and in-situ AFM. We first compare the results obtained from these two techniques and then discuss the factors that control the organic matter's mechanical properties within the shale. We comment on the benefits of using in-situ AFM mapping or in-situ nanoindentation as a standard technique to reveal nano- and micro- mechanical heterogeneities within organic matter.

4.1. Comparison of nanoindentation and AFM data

4.1.1. Mechanical properties

The calculated Young's moduli from nanoindentation are in the range 5.5–6.6 GPa, while those from AFM mapping are 10.0–12.5 GPa (Fig. 7). The modulus values from AFM are up to two times higher than those from the nanoindentation. We identify three possible reasons for these variations. One reason is a different theoretical definition of Young's modulus for organic matter via nanoindentation and AFM (Fig. 1), in nanoindentation, the Young's modulus is calculated from the slope of the initial unloading curve, i.e., S value (Eq. 1). The AFM method determines Young's modulus from the force-distance curves based on the Hertz-Sneddon model (Eq. 4). Second main reason may be the difference in indentation depth and deformation type produced

Table 3
Summary of AFM-determined surface roughness, Young's modulus, adhesive force of representative area parameters for one chosen AFM 10 × 10 μm² map of organic matter shown in Fig. 5 and the corresponding mean parameters from ten AFM (10 × 10 μm²) maps.

Sample	VR_o(%)	R_a (nm)	R_q (nm)	Young's modulus (GPa)		Adhesive force (nN)	
				Ave.	Std.	Ave.	Std.
10 × 10 μm² (one map)							
SQ-81	2.56	7.3	9.3	9.3	1.5	37.6	17.8
SQ-86	2.65	10.2	13.0	10.5	0.8	109.5	50.0
SQ-88	2.76	8.9	11.5	12.4	2.0	94.1	25.0
SQ-89	2.60	3.4	4.5	11.6	1.5	90.9	50.5
10 × 10 μm² (ten maps)							
SQ-81	2.56	15.1 ± 7.9	17.6 ± 6.2	10.0	0.6	37.4	7.8
SQ-86	2.65	11.5 ± 5.3	14.6 ± 6.3	10.2	0.6	91.7	18.8
SQ-88	2.76	8.1 ± 2.2	10.7 ± 2.8	12.5	0.2	98.6	5.2
SQ-89	2.60	4.5 ± 2.1	6.6 ± 3.4	10.8	0.6	67.9	17.7

between the two techniques. Our AFM experiments with a relatively low force (i.e., 8000 nN) typically can probe the ~30 nm-deep deformation zone for organic matter's surface at the nanoscale, therefore could be regarded as a non-destructive technique, with no plastic deformation on the sample (Eliyahu et al., 2015; Emmanuel et al., 2016). In contrast, nanoindentation-based methods produce a deformation at 250–350 nm depth within the organic matter in our samples. The elasto-plastic deformation zone beneath the indenter is 3–5 times h_{max} (Larsson et al., 1996). Thus, the elasto-plastically deformed zone of organic matter by nanoindentation is 750–1750 nm and exceeds the size of most micro-pores (Fig. 1 and Fig. 5). Thus, the Young's moduli determined by nanoindentation and AFM can be affected very differently by the organic matter fabric with pores and/or trapped nanomineral inclusions. Previous studies of organic matter indentation in shales have suggested that the values of calculated mechanical parameters decrease with the increasing penetration depth (Yang et al., 2023). The third main reason is the difference in the spatial resolution and data statistics between the two methods. AFM, with high spatial resolution, can probe the mechanical properties of individual target points (single organic matter particle or possible hard mineral nanoparticles). However, nanoindentation does not have the ability to detect scales as finely as AFM, and the resultant Young's modulus represents a much larger area, where the response of possible mineral nanoparticles and pores is averaged to a much larger extent. This implies that the elastic modulus measured from nanoindentation accounts for the response of the organic matter with nano- and micro-pores, i.e., an aggregate of particles with pores (Fig. 2h), whereas the elastic modulus measured using AFM represents that of the solid organic matter or the possible hard mineral nanoparticles. It has been shown that hard mineral nanoparticles (e.g., pyrite and quartz) can be entrained in organic matter (Galvez et al., 2012; Parnell et al., 1994). When the AFM tip is located on these hard mineral nanoparticles, it yields a larger Young's modulus.

4.1.2. *Spatial resolution and statistics*

The in-situ QI-AFM technique provides a spatially continuous measurement and better statistics of mechanical properties of organic matter when taking the number of data collected into account. Higher spatial resolution (here: 128 × 128 indents over a surface area of 10 × 10 μm²) is one of its superior features and advantages of AFM. Moreover, because the indents are all located on the organic matter, it does not require

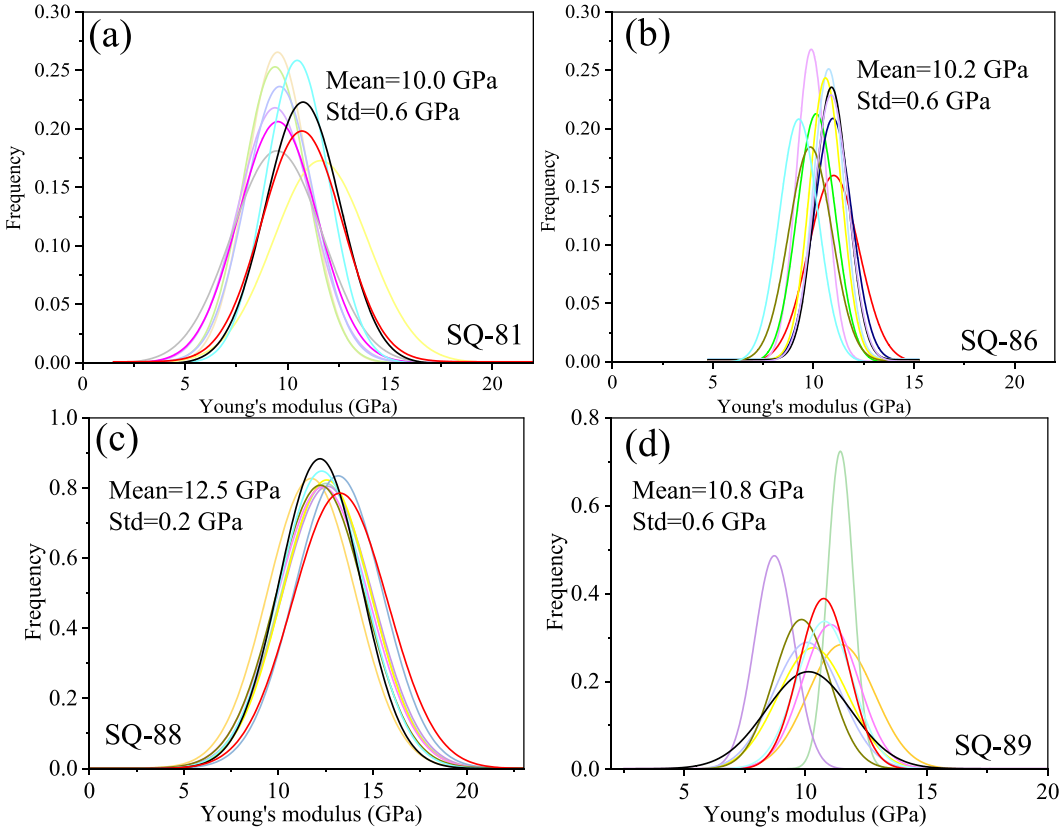

Fig. 6. AFM-determined distribution of Young's modulus measured on ten different non-overlapping areas within the chosen organic matter domain in four shale samples (a) SQ-81, (b) SQ-86, (c) SQ-88, and (d) SQ-89. The maximum force was 8 μN and the loading/unloading speed was 25 μm/s. Each curve represents a Gaussian fit to a histogram of Young's modulus values for one AFM 10 × 10 μm² map corresponding to 128 × 128 indents. The mean and standard deviation (Std) values are calculated from ten different areas.

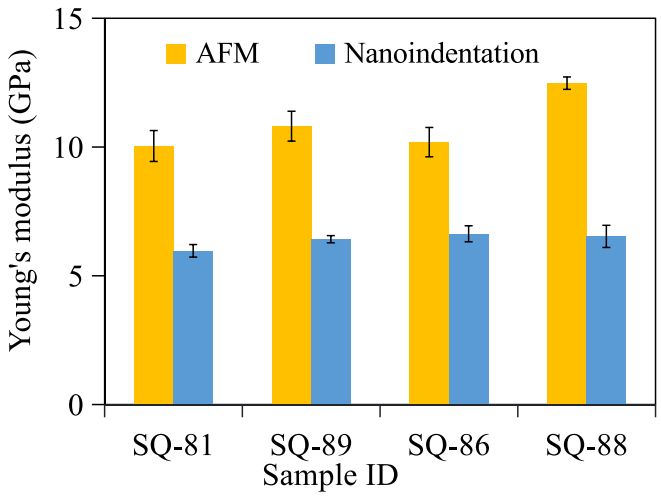

Fig. 7. Comparison of Young's modulus of organic matter measured by AFM and nanoindentation.

choosing the proper indents and can provide true nanometer scale resolution of organic matter. In contrast, the nanoindentation technique applied the indent grids that are spaced several micrometers apart to measure the elastic modulus of organic matter grains. Since the organic matter grains are not always all large, the measurements of nanoindentation on organic matter are confined and the number of measurement points is limited (here: 5 to 14 indents based on the size of organic matter). This means that the micron-scale spatial resolution of Young's modulus from nanoindentation is much lower than in AFM and often provides poorer data statistics. Only if sufficient indents are acquired for nanoindentation tests, the nanoindentation results can be provide a representative picture of the mechanical properties of organic matter within shales.

Due to the low applied force applied and shallow indentation depths in AFM, it is possible to measure the elastic modulus of tiny organic matter grains (<2 μm) in shale, while this is beyond the application scope of nanoindentation, which requires the size of organic matter being larger than 2 μm (Yang et al., 2023). However, with the AFM's microscope is in low resolution, it is very difficult to distinguish the organic matter from other minerals in the shale matrix, especially for shales with low organic content (Fig. 5a). The indentation system equipped with an optical microscope with a maximum magnification of 4000×, is easier to use to locate target organic matter grains (Fig. 2). In addition, under the low force of AFM, the contact between the organic matter and the tip cannot produce a plastic deformation, but it can probe the attraction and repulsion between the tip and the solid (Derjaguin et al., 1975). As such, one can obtain elastic modulus and adhesion (adhesive force) by AFM. Besides, if the shale sample is ion polished well, based on the AFM mapping we can investigate possible pore characteristics of organic matter (Zhao et al., 2019; Li et al., 2020). In contrast, nanoindentation technique is capable of obtaining elastic modulus, hardness (plasticity), fracture toughness, and creep behavior of organic matter in shale at the nanoscale (Slim et al., 2019; Zeszotarski et al., 2004). In summary, in-situ nanoindentation and in-situ AFM tests are complementary approaches to estimate the mechanical properties of organic matter in shale. Considering their respective advantages mentioned above, it is recommended to combine the nanoindentation with AFM to achieve comprehensive mechanical characterization of organic matter.

4.2. Factors influencing the mechanical response of organic matter in the WF-LMX shale

When considering the mechanical properties of the different types of organic matter in the WF-LMX shale, the Young's modulus and hardness of graptolite are slightly larger than those of solid bitumen, which agrees with the fact that kerogen has a larger elastic modulus than bitumen (Table 4). Graptolite and solid bitumen come from primitive organic matter, which have different chemical structures. The thermal responses of these organic materials during geological evolution are different. Solid bitumen is the hydrocarbon products generated from vitrinite (Bernard et al., 2012; Stasiuk, 1997). Compared with vitrinite, graptolite has a higher aromaticity, which may cause it to mature at a rate higher than vitrinite. Therefore, graptolite has a higher reflectivity after the same thermal evolution history, thus explaining its stiffer characteristic. The difference in the maturation process between solid bitumen and graptolite results in an inconsistent change in their reflectivity (Luo et al., 2018) and mechanical properties. Therefore, the Young's moduli and hardness of graptolites with higher reflectivity are also larger than for bitumen.

When considering the effect of maturity of the organic matter in the WF-LMX Formation on the mechanical properties, the Young's modulus and hardness values generally increase with VR_o. Similar results have been in studies of the in-situ organic matter in shales (Table 4 and Fig. 8) and pure organic matter in thermal simulation experiments (Liu et al., 2018; Wang et al., 2022b). The increase of elastic parameters is rather modest in our data: 3.05 GPa for Young's modulus and 0.14 GPa for hardness from VR_o = 2.14% to VR_o = 3.10%, which is also consistent with data on kerogen (Wang et al., 2022b) and solid bitumen (Liu et al., 2018). Previous study has indicated that the variation of stiffness of organic matter with maturity is mainly caused by changes in the chemical structure of organic matter (Emmanuel et al., 2016). The aliphatic carbon groups almost all cleave from organic matter, with the formation of substantial fused aromatic carbons, and shrinkage between aromatic layers for the organic matter at the over-mature stage (Durand, 1980). Because of the incremental aromatization, the organic matter will evolve to stiff graphite-like organic matter with a high density (Duan et al., 2018; Okiongbo et al., 2005), thereby leading to its increasing elastic modulus (Emmanuel et al., 2016).

When considering the effect of anisotropy on mechanical properties of organic matter in the WF-LMX shale, mechanical properties obtained for graptolite particles analyzed along the X1 and X3 bedding planes are relatively close. Although the mechanical properties of solid bitumen from X3 bedding plane were not obtained in this work, the mechanical properties, especially for the Young's modulus, of solid bitumen from X1 bedding plane are close to those of graptolite particles on the X3 bedding plane. This result indicates that the mechanical properties of organic matter in this shale are isotropic or weakly anisotropic. Similar results can be found on mechanical properties of kerogen in Woodford shale (Zeszotarski et al., 2004) and optical characteristics of solid bitumen or pyrobitumen (HéRoux and Tassé, 1990; Mossman et al., 1993). The reason for this result may be related to the isotropic pressure of pore fluids in rock, and the long time of warming under isotropic pressure conditions (Zeszotarski et al., 2004). Thus, more organic-rich shales should be studied to quantify the elastic anisotropy of organic matter.

4.3. Implications and limitations

The accurate testing and characterization of in-situ mechanical properties of organic matter in shale can be helpful to develop rock mechanical models to the accurate evaluation of the actual mechanical properties of shale. Compared to previous grid indentation or AFM technique (Table 4), the in-situ AFM testing produces more accurate and intrinsic mechanical properties of organic matter. The parameters of the organic matter phase based on the deconvolution results from nanoindentation are actually those of a mixture of clay minerals and organic matter. Thus the overall range of elastic modulus (e.g., 4–23 GPa) for organic matter phase is larger from nanoindentation data compared to the AFM results (e.g., 8–16 GPa) (Kong et al., 2021). The large standard deviation (8.78 ± 3.09 GPa) of elastic modulus for organic matter phase

Table 4
Mechanical properties of organic matter measured by AFM and/or nanoindentation (previous studies).

Literature	Maturity	Kerogen			Bitumen	Formation	methodology
		φ	*E* (GPa)	*H* (GPa)	*E* (GPa)		
Kumar et al. (2012)	R_o = 0.54%	11.8%	2.0 ± 0.2	0.14 ± 0.01	/	Woodford	In-situ nanoindentation
		0	8.7 ± 1.0	0.9 ± 0.1			
	R_o = 0.9%	0	6.9 ± 1.2	0.55 ± 0.08			
	R_o = 1.61%	Low	7.6 ± 1.3	0.68 ± 0.14			
	R_o = 3.6%	5.8%	4.7 ± 2.4	0.39 ± 0.36			
	R_o = 6.36%	0	15.3 ± 1.5	2.0 ± 0.6			
Shukla et al. (2013)	R_o = 0.37–0.53%	/	5.6	0.2	/	Kimmeridge	In-situ nanoindentation
	R_o = 0.54%	low	8.7	0.9		Woodford	
		High	2	0.14			
	R_o = 1.61%	0	7.6	0.5			
Zargari et al. (2016)[a]	Onset of oil generation: HI = 633(mg HC/g TOC), T_{max}: 428°C[a]	Low	15–20		/	Bakken	Grid nanoindentation
	Peak of oil generation: HI = 126–257 (mg HC/g TOC), T_{max}:442–457°C[b]	High	7–10	/			
	Gas window:HI = 6 (mg HC/g TOC)[c]	High	7–12				
Zeszotarski et al. (2004)	T_{max}:421°C[d]	/	10.5–11.1	0.55–0.57	/	Woodford	In-situ nanoindentation
Bennett et al. (2015)	Oil window:(Ro <1.0%)	/	6.2–10.7	0.28–0.31		Woodford	Grid nanoindentation
Zargari et al. (2013)	Gas window:HI = 35.6–79.0 (mg /g TOC)[e]		8.5–23.5	/	<2	Bakken	Grid nanoindentation
Emmanuel et al. (2016)	R_o = 0.40%	/	6.1		/	Cretaceous Source Rock	AFM (PF-QNM)
	R_o = 0.82%	/	16	/	7.5		
	R_o = 1.25%	/	15.8		8.5		
Eliyahu et al. (2015)	R_o = 2.1%	/	15.5 ± 0.5	/	/	Upper Jurassic source rock	AFM (PF-QNM)
Khatibi et al. (2018)	R_o = 0.54%	/	2.5	/	/	Bakken	AFM (PF-QNM)
	R_o = 0.59%	/	4				
	R_o = 0.86%	/	4.2				
	R_o = 0.92%	/	5.35				
	R_o = 0.94%	/	16				
Li et al. (2018b)	R_o = 0.35%	/	2.91	/	/	Bakken	AFM (PF-QNM)
	R_o = 0.64%	/	/		3.3		
	R_o = 1.04%	/	/		11.7		
Li et al. (2018c)	R_o = 0.54%		10–20	/	/	Bakken	AFM (PF-QNM)
	R_o = 0.62%		7.3–14.6	/	/		
	R_o = 0.93%		7.3–22.8	/	/		
	R_o = 1.04%		9.1–18.2	/	/		
Zhao et al. (2020)	R_o = 0.62%	/	3.5–5.2	/	/	Shahejie	In-situ nanoindentation
	R_o = 0.69%	/	4.7–6.0		3.2		
	R_o = 0.94%	/	5.5–7.5		3.5		
	R_o = 1.13%	/	6.3–8.3		5.6		
Fender et al. (2020)	T_{max}:442–457°C[f]	/	0.1–23	/	/	Barnett	QI-AFM
	T_{max}:464°C[g]	/	0.1–24	/	/	Bowland	
	T_{max}:443.5–457°C[h]	/	0.1–20	/	/	Engle Ford	
	T_{max}:408°C[i]	/	0.1–14	/	/	Tarfaya	
Kong et al. (2021)	T_{max}:428°C[j]	/	4–23	/	/	Bakken	Grid nanoindentation
		/	8–16	/	/		AFM (PF-QNM)
	T_{max}:432°C[k]	/	1–30	/	/		Grid nanoindentation
		/	10–25	/	/		AFM (PF-QNM)
	T_{max}:445°C[l]	/	2–35	/	/		Grid nanoindentation
		/	1–30	/	/		AFM (PF-QNM)
	T_{max}:450°C[m]	/	5–53	/	/		Grid nanoindentation
		/	10–25	/	/		AFM (PF-QNM)
Tan et al. (2021)	R_o = 0.98–1.28%	/	8.2–13.9	/	/	/	AFM (PF-QNM)
Zhang et al. (2022)	R_o = 0.52–1.45%	/	3.0–13.9	/	/	Fengcheng and Lucaogou	AFM (PF-QNM)
Yang et al. (2023)	R_o = 2.60%	0	7.0–7.5	0.8–0.9	/	Longmaxi	In-situ nanoindentation
		high	4.5–5.5	0.3–0.4	/		
		moderate	/	/	6.6 (*H*:0.5–0.6)		

[a] Modulus in this literature is storage modulus; Organic porosity = φ. The equilibrium vitrinite reflectance (R_o) is calculated using the T_{max} analyzed by Rock-Eval (Jarvie et al., 2001): $R_o\% = 0.018 \times T_{max} - 7.16$. a: $R_o = 0.5\%$, b: $R_o = 0.8$–1.1%, c: $R_o \approx 1.8\%$, d: $R_o = 0.4\%$, e: $R_o \approx 1.8\%$, f: $R_o = 0.8$–1.1%, g: $R_o = 1.2\%$, h: $R_o = 0.8$–1.1%, i: $R_o = 0.2\%$, j: $R_o = 0.5\%$, k: $R_o = 0.6\%$, l: $R_o = 0.8\%$, m: $R_o = 0.9\%$.

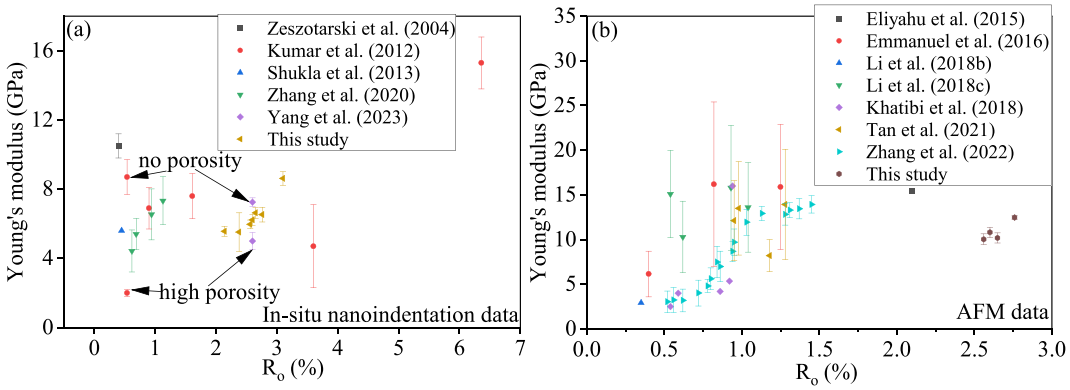

Fig. 8. Plot of Young's modulus of organic matter versus maturation (R_o) according to the present and previous studies. (a) Young's modulus from in-situ nanoindentation method vs R_o; (b) Young's modulus from all the AFM methods vs R_o. The data of organic matter here is from kerogen. Error bars show one standard deviation.

in shale (Bennett et al., 2015) may reflect a lower spatial resolution of this method. Previous studies have also attempted to upscale the mechanical property from shale matrix components to the bulk shale, and the upscaled Young's modulus is slightly larger (Shi et al., 2019) or not completely consistent with that from triaxial compressions test (Li et al., 2021), which may be caused by that the influence of organic matter was not considered. Although most shale mainly contains clay and hard minerals such as quartz and feldspar, for some highly organic shale (e.g., TOC content>10%), accurate testing of the mechanical properties of organic matter is crucial to the development of upscaling model.

Organic matter is not only the source material of shale oil/gas, but also provides storage space for shale oil/gas reservoirs, and its high content also significantly influences the macroscopic mechanical properties of shale, thereby affecting the exploration and development of shale oil/gas. During the thermal evolution process, its mechanical property can vary. The maturity range of organic matter in shale selected in this study is relatively small (2.14–3.10%). Although Table 4 and Fig. 8 summarize the relationship between the mechanical properties of organic matter in different formation shales and maturity, and the change of mechanical properties with maturity for organic matter from immature to over mature stage was also simulated by thermal simulation experiments (Liu et al., 2018; Wang et al., 2022b), the evolution of organic matter's mechanical properties in actual geological condition with maturity needs to be explored throughout the entire thermal evolution process. On the other hand, due to the relatively low TOC in some samples and the difficulty in finding organic matter under AFM microscopy, only four samples were explored here to study the relationship between the mechanical properties or adhesive force and maturity. In the future, more organic-rich shale with a wider maturity range will be needed for quantitative research between them.

Finally, WF-LMX shale gas reservoirs are generally located up 2000–3000 m depth (Guo and Zhang, 2014; Yang et al., 2016), where temperature, pressure and fluid are significantly different from the ambient conditions where the nanoindentation data were acquired. Therefore, the obtained mechanical property of organic matter is not fully representative of that in the actual subsurface formation. It has been reported that the elastic modulus of bitumen decreases from 5.9 GPa at 25 °C to 0.8 GPa at 225 °C, while that of kerogen keeps almost constant (i.e., 39 GPa) from 25 °C to 150 °C (Emmanuel et al., 2017), indicating the different thermal response of kerogen and bitumen when temperature conditions vary. Nanoindentation with heat device has been applied to study the mechanical properties of shales (Espinoza et al., 2022; Wang et al., 2021), granite (Mo et al., 2022) and graphite crystals (Marrow et al., 2022). Considering the restricted experimental conditions, our tests were conducted without involving the influences of temperature and fluids. Details of the mechanical properties of organic matter in the shale under actual geological conditions should be stimulated in future studies.

5. Conclusions

We used high-resolution in-situ AFM and nanoindentation measurements, to quantitatively reveal the nanomechanical properties of organic matter in the marine WF-LMX Formation shale samples. We compared the results from the two methods and discussed their merits and limitations. The following conclusions can be drawn:

(1) In-situ nanoindentation and in-situ AFM techniques are both more accurate approaches to estimate the mechanical properties of organic matter in shale than traditional grid indentation methods. Nanoindentation makes it straightforward to find and locate the organic matter, and produce not only Young's moduli and hardness, but also creep behavior of organic matter. AFM technique is capable of obtaining, the elastic modulus and adhesion properties of tiny organic matter grains, and has a higher spatial resolution. Considering their respective advantages mentioned, we recommend combining the nanoindentation with AFM to obtain mechanical properties of organic matter.
(2) The Young's moduli of organic matter calculated from nanoindentation are around twice smaller than those obtained from AFM measurements mainly because the elasto-plastic deformation zone of organic matter in nanoindentation tests is larger and can be additionally affected by the presence of inorganic particles and/or larger micro-pores in organic matter.
(3) The Young's moduli and hardness of graptolite in shale are slightly larger than those of solid bitumen. The mechanical properties of organic matter in WF-LMX Formation shales are isotropic or weakly anisotropic. If we neglect the impact of organic matter type, the Young's modulus and hardness of organic matter in WF-LMX Formation shales increase moderately with maturity.

Author statement

This manuscript or a very similar manuscript has not been published, nor is under consideration by any other journal.

CRediT authorship contribution statement

Jianfeng Wang: Conceptualization, Data curation, Investigation, Methodology, Visualization, Writing – original draft, Writing – review & editing. **Joanna Dziadkowiec:** Conceptualization, Data curation, Investigation, Methodology, Supervision, Writing – original draft, Writing – review & editing. **Yuke Liu:** Investigation, Methodology. **Wenmin Jiang:** Data curation, Methodology. **Yijun Zheng:** Methodology. **Yongqiang Xiong:** Supervision, Writing – original draft, Funding acquisition. **Ping'an Peng:** Supervision. **François Renard:** Methodology, Supervision, Writing – original draft, Writing – review & editing.

Declaration of Competing Interest

The authors declare that they have no known competing financial interests or personal relationships that could have appeared to influence the work reported in this paper.

Data availability

Data will be made available on request.

Acknowledgements

This research was supported by the Special Fund for the Strategic Priority Research Program of the Chinese Academy of Sciences (Grant XDA14010102). The project was also funded by the Njord Centre at the University of Oslo. The support provided by the University of the Chinese Academy of Sciences during a visit of Dr. Jianfeng Wang to the University of Oslo is acknowledged. Thanks also extend to Prof. Yuhong Liao for providing the shale samples. We are very grateful to Editor Dr. Deolinda Flores, Dr. Aaron M. Jubb and one anonymous reviewer for their constructive comments that significantly improve this manuscript. This is contribution No.IS-3426 from GIGCAS.

Appendix A. Supplementary data

Supplementary data to this article can be found online at https://doi.org/10.1016/j.coal.2023.104406.

References

Abouelatta, O.B., Mádl, J., 2001. Surface roughness prediction based on cutting parameters and tool vibrations in turning operations. J. Mater. Process. Technol. 118, 269–277.
Ahmadov, R., Vanorio, T., Mavko, G., 2009. Confocal laser scanning and atomic-force microscopy in estimation of elastic properties of the organic-rich Bazhenov Formation. Lead. Edge 28, 18–23.
Allen, M., Faulkner, D., Worden, R., Rice-Birchall, E., Katirtsidis, N., Utley, J., 2020. Geomechanical and petrographic assessment of a CO2 storage site: Application to the Acorn CO2 storage site, offshore United Kingdom. Int. J. Greenhouse Gas Control 94, 102923.
Alstadt, K.N., Katti, K.S., Katti, D.R., 2015. Nanoscale Morphology of Kerogen and in Situ Nanomechanical Properties of Green River Oil Shale. J. Nanomech. Micromech. 6, 04015003.
Bennett, K.C., Berla, L.A., Nix, W.D., Borja, R.I., 2015. Instrumented nanoindentation and 3D mechanistic modeling of a shale at multiple scales. Acta Geotech. 10, 1–14.
Bernard, S., Wirth, R., Schreiber, A., Schulz, H.-M., Horsfield, B., 2012. Formation of nanoporous pyrobitumen residues during maturation of the Barnett Shale (Fort Worth Basin). Int. J. Coal Geol. 103, 3–11.
Bertrand, Y., 1987. Chitinozoan, Graptolite, and Scolecodont Reflectance as an Alternative to Vitrinite and Pyrobitumen Reflectance in Ordovician and Silurian Strata, Anticosti Island, Quebec, Canada. AAPG Bull. 71, 951–957.
Charlton, T.S., Goodarzi, M., Rouainia, M., Aplin, A.C., Cubillas, P., 2021. Effect of Diagenesis on Geomechanical Properties of Organic-Rich Calcareous Shale: a Multiscale Investigation. J. Geophys. Res.: Solid Earth 126, 1-23 e2020JB021365.
Charlton, T., Rouainia, M., Aplin, A., Fisher, Q., Bowen, L., 2023. Nanoindentation of Horn River Basin Shales: the micromechanical contrast between overburden and reservoir formations. J. Geophys. Res.: Solid. Earth 128 e2022JB025957.
Davis, C.A., 1900. A contribution to the natural history of marl. J. Geol. 8, 485–497.
Derjaguin, B.V., Muller, V.M., Toporov, Y.P., 1975. Effect of contact deformations on the adhesion of particles. J. Colloid Interface Sci. 53, 314–326.
Du, J., Whittle, A.J., Hu, L., Divoux, T., Meegoda, J.N., 2021. Characterization of meso-scale mechanical properties of Longmaxi shale using grid microindentation experiments. J. Rock Mech. Geotech. Eng. 13, 555–567.
Duan, D., Zhang, D., Ma, X., Yang, Y., Ran, Y., Mao, J., 2018. Chemical and structural characterization of thermally simulated kerogen and its relationship with microporosity. Mar. Pet. Geol. 89, 4–13.
Durand, B., 1980. Sedimentary Organic Matter and Kerogen. Definition and Quantitative Importance of Kerogen. Kerogen: Insoluble Organic Matter from Sedimentary Rocks. Editions Technip, pp. 13–34.
Eliyahu, M., Emmanuel, S., Day-Stirrat, R.J., Macaulay, C.I., 2015. Mechanical properties of organic matter in shales mapped at the nanometer scale. Mar. Pet. Geol. 59, 294–304.
Emmanuel, S., Eliyahu, M., Day-Stirrat, R.J., Hofmann, R., Macaulay, C.I., 2016. Impact of thermal maturation on nano-scale elastic properties of organic matter in shales. Mar. Pet. Geol. 70, 175–184.
Emmanuel, S., Eliyahu, M., Day-Stirrat, R.J., Hofmann, R., Macaulay, C.I., 2017. Softening of organic matter in shales at reservoir temperatures. Pet. Geosci. 23, 262–269.
Espinoza, W.F., Zhang, F., Dai, S., 2022. Impacts of temperature on the mechanical properties of Longmaxi shale outcrops using instrumented nanoindentation. Geomech. Energy Environ. 30, 100348.
Fender, T.D., Van Der Land, C., Rouainia, M., Graham, S.P., Jones, D.M., Vane, C.H., Wagner, T., 2020. The assessment of organic matter young's modulus distribution with depositional environment and maturity. J. Geophys. Res. Solid Earth 125 e2020JB020435.
Gadelmawla, E.S., Koura, M.M., Maksoud, T.M.A., Elewa, I.M., Soliman, H.H., 2002. Roughness parameters. J. Mater. Process. Technol. 123, 133–145.
Galvez, M.E., Beyssac, O., Benzerara, K., Menguy, N., Bernard, S., Cox, S.C., 2012. Micro- and nano-textural evidence of Ti(–Ca–Fe) mobility during fluid–rock interactions in carbonaceous lawsonite-bearing rocks from New Zealand. Contrib. Mineral. Petrol. 164, 895–914.
Gao, Y., Liu, B., Fu, X., Tian, S., Wang, B., Wang, L., Gentzis, T., Ostadhassan, M., 2023. Nanomechanical and chemical variations of inertinite and vitrinite within lacustrine shale during oil generation. Mar. Pet. Geol. 154, 106318.
Goodarzi, F., 1984. Organic petrography of graptolite fragments from Turkey. Mar. Pet. Geol. 1, 202–210.
Graham, S., Rouainia, M., Aplin, A., Cubillas, P., Fender, T., Armitage, P., 2021. Geomechanical characterisation of organic-rich calcareous shale using AFM and nanoindentation. Rock Mech. Rock. Eng. 54, 303–320.
Guo, T., Zhang, H., 2014. Formation and enrichment mode of Jiaoshiba shale gas field, Sichuan Basin. Pet. Explor. Dev. 41, 31–40.
HéRoux, Y., Tassé, N., 1990. Organic-matter alteration in an early Paleozoic basin: Zonation around mineral showings compared to that around intrusions, St. Lawrence Lowlands, Quebec, Canada. GSA Bull. 102, 877–888.
Hertz, H., 1882. Ueber die Berührung fester elastischer Körper. 1882, 156–171.
Hou, C., Jiang, B., Liu, H., Song, Y., Xu, S., 2020. The differences of nanoscale mechanical properties among coal maceral groups. J. Nat. Gas Sci. Eng. 80, 103394.
Hutton, A.C., 1987. Petrographic classification of oil shales. Int. J. Coal Geol. 8, 203–231.
Jarvie, D.M., Claxton, B.L., Henk, F., Breyer, J.T., 2001. Oil and shale gas from the Barnett shale, Fort Worth basin, Texas, 10. Am. Assoc. Petroleum Geologists A100.
Khatibi, S., Ostadhassan, M., Tuschel, D., Gentzis, T., Bubach, B., Carvajal-Ortiz, H., 2018. Raman spectroscopy to study thermal maturity and elastic modulus of kerogen. Int. J. Coal Geol. 185, 103–118.
Kong, L., Hadavimoghaddam, F., Li, C., Liu, K., Liu, B., Semnani, A., Ostadhassan, M., 2021. AFM vs. Nanoindentation: Nanomechanical properties of organic-rich Shale. Mar. Pet. Geol. 132, 105229.
Kossovich, E.L., Dobryakova, N.N., Epshtein, S.A., Belov, D.S., 2016. Mechanical properties of coal microcomponents under continuous indentation. J. Min. Sci. 52, 906–912.
Kumar, V., Curtis, M., Gupta, N., Sondergeld, C., Rai, C., 2012. Estimation of elastic properties of organic matter in woodford shale through nanoindentation measurements. Society of Petroleum Engineers - SPE Canadian Unconventional Resources Conference 2012.
Larsson, P.L., Giannakopoulos, A.E., Sderlund, E., Rowcliffe, D.J., Vestergaard, R., 1996. Analysis of Berkovich indentation. Int. J. Solids Struct. 33, 221–248.
Lévy, R., Maaloum, M., 2002. Measuring the spring constant of atomic force microscope cantilevers: thermal fluctuations and other methods. Nanotechnology 13, 33–37.
Li, C., Ostadhassan, M., Abarghani, A., Fogden, A., Kong, L., 2018a. Multi-scale evaluation of mechanical properties of the Bakken shale. J. Mater. Sci. 54, 2133–2151.
Li, C., Ostadhassan, M., Gentzis, T., Kong, L., Carvajal-Ortiz, H., Bubach, B., 2018b. Nanomechanical characterization of organic matter in the Bakken formation by microscopy-based method. Mar. Pet. Geol. 96, 128–138.
Li, C., Ostadhassan, M., Guo, S., Gentzis, T., Kong, L., 2018c. Application of PeakForce tapping mode of atomic force microscope to characterize nanomechanical properties of organic matter of the Bakken Shale. Fuel 233, 894–910.
Li, Y., Yang, J., Pan, Z., Tong, W., 2020. Nanoscale pore structure and mechanical property analysis of coal: an insight combining AFM and SEM images. Fuel 260, 116352.
Li, C., Wang, D., Kong, L., 2021. Mechanical response of the Middle Bakken rocks under triaxial compressive test and nanoindentation. Int. J. Rock Mech. Min. Sci. 139, 104660.
Link, C.M., Bustin, R., Goodarzi, F., 1990. Petrology of graptolites and their utility as indices of thermal maturity in lower Paleozoic strata in northern Yukon. Canada. Int. J. Coal Geol. 15, 113–135.

Liu, Y., Xiong, Y., Li, Y., Peng, P.A., 2018. Effect of thermal maturation on chemical structure and nanomechanical properties of solid bitumen. Mar. Pet. Geol. 92, 780–793.
Liu, Y., Sokolov, I., Dokukin, M.E., Xiong, Y., 2020. Can AFM be used to measure absolute values of Young's modulus of nanocomposite materials down to the nanoscale? Nanoscale 12 (23), 12432–12443.
Luo, Q., Hao, J., Skovsted, C.B., Xu, Y., Liu, Y., Wu, J., Zhang, S., Wang, W., 2018. Optical characteristics of graptolite-bearing sediments and its implication for thermal maturity assessment. Int. J. Coal Geol. 195, 386–401.
Marrow, T.J., Šulak, I., Li, B.S., Vukšić, M., Williamson, M., Armstrong, D.E.J., 2022. High temperature spherical nano-indentation of graphite crystals. Carbon 191, 236–242.
Mighani, S., Bernabé, Y., Boulenouar, A., Mok, U., Evans, B., 2019. Creep Deformation in Vaca Muerta Shale from Nanoindentation to Triaxial experiments. J. Geophys. Res.: Solid. Earth 124, 7842–7868.
Mo, C., Zhao, J., Zhang, D., 2022. Real-Time Measurement of Mechanical Behavior of Granite During Heating–Cooling Cycle: A Mineralogical Perspective. Rock Mech. Rock. Eng. 55, 4403–4422.
Mossman, D.J., Nagy, B., Davis, D.W., 1993. Hydrothermal alteration of organic matter in uranium ores, Elliot Lake, Canada: Implications for selected organic-rich deposits. Geochim. Cosmochim. Acta 57, 3251–3259.
Okiongbo, K., C, A.A., Larter, S.R., 2005. Changes in Type II Kerogen Density as a Function of Maturity: evidence from the Kimmeridge Clay Formation. Energy&Fuels 19, 2495–2499.
Oliver, W.C., Pharr, G.M., 1992. An improved technique for determining hardness and elastic modulus using load and displacement sensing indentation experiments. J. Mater. Res. 7, 1564–1583.
Oliver, W.C., Pharr, G.M., 2004. Measurement of hardness and elastic modulus by instrumented indentation: advances in understanding and refinements to methodology. J. Mater. Res. 19, 3–20.
Parnell, J., Carey, P., Bottrell, S., 1994. The Occurrence of Authigenic Minerals in Solid Bitumens. J. Sediment. Res. 64, 95–100.
Sauerer, B., Stukan, M., Abdallah, W., Derkani, M., Fedorov, M., Buiting, J., Zhang, Z., 2016. Quantifying Mineral Surface Energy by Scanning Force Microscopy. J. Colloid Interface Sci. 472, 237–246.
Schoenherr, J., Littke, R., Urai, J.L., Kukla, P.A., Rawahi, Z., 2007. Polyphase thermal evolution in the Infra-Cambrian Ara Group (South Oman Salt Basin) as deduced by maturity of solid reservoir bitumen. Org. Geochem. 38, 1293–1318.
Shi, X., Jiang, S., Lu, S., He, Z., Li, D., Wang, Z., Xiao, D., 2019. Investigation of mechanical properties of bedded shale by nanoindentation tests: a case study on lower Silurian Longmaxi Formation of Youyang area in Southeast Chongqing. China. Pet. Explor. Dev. 46, 163–172.
Shukla, P., Kumar, V., Curtis, M., Sondergeld, C.H., Rai, C.S., 2013. Nanoindentation Studies on Shales. In: 47th U.S. Rock Mechanics/Geomechanics Symposium, San Francisco, California. ARMA-2013-2578.
Slim, M., Abedi, S., Bryndzia, L.T., Ulm, F.-J., 2019. Role of Organic Matter on Nanoscale and Microscale Creep Properties of Source Rocks. J. Eng. Mech. 145, 04018121.
Sneddon, I.N., 1965. The relation between load and penetration in the axisymmetric boussinesq problem for a punch of arbitrary profile. Int. J. Eng. Sci. 3, 47–57.
Stasiuk, L.D., 1997. The origin of pyrobitumens in upper Devonian Leduc formation gas reservoirs, Alberta, Canada: an optical and EDS study of oil to gas transformation. Mar. Pet. Geol. 14, 915–929.
Tan, X., Gilliland, E., Tang, X., Ripepi, N., 2020. Integrated Experimental Characterization of Shales of varying thermal Maturation in the Central Appalachian Basin using Raman and Fourier Transform infrared Spectroscopy and Atomic Force Microscopy. Energy Fuel 35, 201–212.
Tian, X., He, X., Song, D., Li, Z., Khan, M., Liu, H., Qiu, L., 2022. AFM characterization of surface mechanical and electrical properties of some common rocks. Int. J. Min. Sci. Technol. 32, 435–445.
Valentine, B.J., Hackley, P.C., 2023. Scanning electron microscopic evaluation of broad ion beam milling effects to sedimentary organic matter: Sputter-induced artifacts or naturally occurring porosity? Int. J. Coal Geol. 277, 104348.
Vranjes-Wessely, S., Misch, D., Schöberl, T., Kiener, D., Gross, D., Sachsenhofer, R., 2018. Nanoindentation study of macerals in coals from the Ukrainian Donets Basin. Adv. Geosci. 45, 73–83.
Vranjes-Wessely, S., Misch, D., Kiener, D., Cordill, M.J., Frese, N., Beyer, A., Horsfield, B., Wang, C., Sachsenhofer, R.F., 2021. High-speed nanoindentation mapping of organic matter-rich rocks: a critical evaluation by correlative imaging and machine learning data analysis. Int. J. Coal Geol. 247, 103847.
Wang, Y., Porter, D.L., Naleway, S.E., Newell, P., 2021. Thermo-mechanical characterization of shale using nanoindentation. Sci. Rep. 11, 1–12.
Wang, J., Liu, Y., Yang, C., Jiang, W., Li, Y., Xiong, Y., 2022a. Modeling the Viscoelastic Behavior of Quartz and Clay Minerals in Shale by Nanoindentation Creep Tests. Geofluids 2860077.
Wang, J., Liu, Y., Yang, C., Jiang, W., Li, Y., Xiong, Y., Peng, P.A., 2022b. Evolution of mechanical properties of kerogen with thermal maturity. Mar. Pet. Geol. 145, 105906.
Wang, J., Yang, C., Liu, Y., Li, Y., Xiong, Y., 2022c. Using Nanoindentation to Characterize the Mechanical and Creep Properties of Shale: load and Loading Strain Rate Effects. ACS Omega 7, 14317–14331.
Wang, J., Liu, Y., Yang, C., Zheng, Y., Jiang, W., Menegon, L., Renard, F., Peng, P.A., Xiong, Y., 2023. Upscaling the creep behavior of clay-rich and quartz-rich shales from nanoindentation measurements: Application to the Wufeng-Longmaxi shale, China. Int. J. Rock Mech. Min. Sci. 171, 105580.
Yang, R., He, S., Yi, J., Hu, Q., 2016. Nano-scale pore structure and fractal dimension of organic-rich Wufeng-Longmaxi shale from Jiaoshiba area, Sichuan Basin: Investigations using FE-SEM, gas adsorption and helium pycnometry. Mar. Pet. Geol. 70, 27–45.
Yang, C., Xiong, Y., Wang, J., Li, Y., Jiang, W., 2020a. Mechanical characterization of shale matrix minerals using phase-positioned nanoindentation and nano-dynamic mechanical analysis. Int. J. Coal Geol. 229, 103571.
Yang, C., Xiong, Y., Zhang, J., 2020b. A comprehensive re-understanding of the OM-hosted nanopores in the marine Wufeng–Longmaxi shale formation in South China by organic petrology, gas adsorption, and X-ray diffraction studies. Int. J. Coal Geol. 218, 103362.
Yang, C., Liu, Y., Wang, J., Wu, D., Liu, L., Su, Z., Xiong, Y., 2023. Application of nanoindentation technique in mechanical characterization of organic matter in shale: Attentive issues, test protocol, and technological prospect. Gas Sci. Eng. 113, 204966.
Yu, H., Zhang, Y., Lebedev, M., Han, T., Verrall, M., Wang, Z., Al-Khdheeawi, E., Al-Yaseri, A., Iglauer, S., 2018. Nanoscale geomechanical properties of Western Australian coal.J. Pet. Sci. Eng. 162, 736–746.
Zargari, S., Prasad, M., Mba, K.C., Mattson, E.D., 2013. Organic maturity, elastic properties, and textural characteristics of self resourcing reservoirs. Geophysics 78, D223–D235.
Zargari, S., Wilkinson, T.M., Packard, C.E., Prasad, M., 2016. Effect of thermal maturity on elastic properties of kerogen. Geophysics 81, M1–M6.
Zeszotarski, J.C., Chromik, R.R., Vinci, R.P., Messmer, M.C., Michels, R., Larsen, J.W., 2004. Imaging and mechanical property measurements of kerogen via nanoindentation. Geochim. Cosmochim. Acta 68, 4113–4119.
Zhang, R., Cao, J., Hu, W., Zuo, Z., Yao, S., Xiang, B., Ma, W., He, D., 2022. Nanomechanical characterization of organic-matter maturity by atomic force microscopy. Int. J. Coal Geol. 104094.
Zhao, S., Li, Y., Wang, Y., Ma, Z., Huang, X., 2019. Quantitative study on coal and shale pore structure and surface roughness based on atomic force microscopy and image processing. Fuel 244, 78–90.
Zhao, J., Zhang, W., Zhang, D., Wei, R., Wang, Y., 2020. Influence of Geochemical Features on the Mechanical Properties of Organic Matter in Shale. J. Geophys. Res.: Solid Earth 125 e2020JB019809.
Zheng, Y., Liao, Y., Wang, Y., Xiong, Y., Peng, P.A., 2018. Organic geochemical characteristics, mineralogy, petrophysical properties, and shale gas prospects of the Wufeng–Longmaxi shales in Sanquan Town of the Nanchuan District, Chongqing. AAPG Bull. 102, 2239–2265.